Journal of The Electrochemical Society

The Electrochemical Society
Advancing solid state & electrochemical science & technology

OPEN ACCESS

Modeling How Interface Geometry and Mechanical Stress Affect Li Metal/Solid Electrolyte Current Distributions

To cite this article: Eric A. Carmona and Paul Albertus 2023 *J. Electrochem. Soc.* **170** 020524

View the article online for updates and enhancements.

You may also like

- Multiple-view, Multiple-selection Visualization of Simulation Geometry in CMS
L A T Bauerdick, G Eulisse, C Jones et al.
- Júlio C Fabris
- Investigation of geometrical and scoring grid resolution for Monte Carlo dose calculations for IMRT
B De Smedt, B Vanderstraeten, N Reynaert et al.

Investigate your battery materials under defined force!
The new PAT-Cell-Force, especially suitable for solid-state electrolytes!

- Battery test cell for force adjustment and measurement, 0 to 1500 Newton (0-5.9 MPa at 18mm electrode diameter)
- Additional monitoring of gas pressure and temperature

www.el-cell.com +49 (0) 40 79012 737 sales@el-cell.com

EL-CELL®
electrochemical test equipment

This content was downloaded from IP address 129.2.89.73 on 20/09/2023 at 18:29

Journal of The Electrochemical Society, 2023 **170** 020524

Modeling How Interface Geometry and Mechanical Stress Affect Li Metal/Solid Electrolyte Current Distributions

Eric A. Carmona[*] **and Paul Albertus**[**,z]

Department of Chemical and Biomolecular Engineering, University of Maryland, College Park, Maryland 20742, United States of America

We develop a coupled electrochemical-mechanical model to assess the current distributions at Li/single-ion conducting solid ceramic electrolyte interfaces containing a parameterized interfacial geometric asperity, and carefully distinguish between the thermodynamic and kinetic effects of interfacial mechanics on the current distribution. We find that with an elastic-perfectly plastic model for Li metal, and experimentally relevant mechanical initial and boundary conditions, the stress variations along the interface for experimentally relevant stack pressures and interfacial geometries are small (e.g., <1 MPa), resulting in a small or negligible influence of the interfacial mechanical state on the interfacial current distribution for both plating and stripping. However, we find that the current distribution is sensitive to interface geometry, with sharper (i.e., smaller tip radius of curvature) asperities experiencing greater current focusing. In addition, the effect on the current distribution of an identically sized lithium peak vs valley geometry is not the same. These interfacial geometry effects may lead to void formation on both stripping and plating and at both Li peaks and valleys. The presence of high-curvature interface geometry asperities provides an additional perspective on the superior cycling performance of flat, film-based separators (e.g., sputtered LiPON) versus particle-based separators (e.g., polycrystalline LLZO) in some conditions.

© 2023 The Author(s). Published on behalf of The Electrochemical Society by IOP Publishing Limited. This is an open access article distributed under the terms of the Creative Commons Attribution 4.0 License (CC BY, http://creativecommons.org/licenses/by/4.0/), which permits unrestricted reuse of the work in any medium, provided the original work is properly cited. [DOI: 10.1149/1945-7111/acb8e3]

Manuscript submitted December 7, 2022; revised manuscript received January 13, 2023. Published February 20, 2023.

Supplementary material for this article is available online

List of Symbols

Symbol	Definition
k	Curvature
LLZO	$Li_{6.5}La_3Zr_{1.5}Ta_{0.5}O_{12}$
p	Pressure
SSB	Solid State Battery
α_a	Anodic Charge Transfer Coefficient
α_c	Cathodic Charge Transfer Coefficient
γ	Surface Energy
$\Delta\mu_{e^-}$	Electron Electrochemical Potential
η_s	Surface Overpotential
σ	Stress
$\bar{\bar{\tau}}$	Deviatoric Stress
σ_n	Normal Stress
Ω	Molar Volume
t^+	Cation Transference Number
U	Equilibrium Potential
ϕ	Potential
η_s	Surface Overpotential

Model Parameters

Symbol	Name	Value	Units
G_{Li}	Lithium Shear Modulus	3.4	GPa
G_{Elec}	Electrolyte Shear Modulus	60	GPa
$\sigma_{y,Li}$	Yield Strength	0.7	MPa
σ_{Li}	Lithium Electronic Conductivity	$1.1{\cdot}10^7$	$S{\cdot}cm^{-1}$
i_o	Exchange Current Density	Varied	$mA{\cdot}cm^{-2}$
κ_{Elec}	Electrolyte Ionic Conductivity	Varied 10^{-6}–10^{-2}	$S{\cdot}cm^{-1}$
ν_{Li}	Lithium Poisson's Ratio	0.42	—
ν_{Elec}	Electrolyte Poisson's Ratio	0.30	—

*Electrochemical Society Student Member.
**Electrochemical Society Member.
[z]E-mail: albertus@umd.edu

(Continued).

Model Parameters

Symbol	Name	Value	Units
Ω_{Li}	Lithium Molar Volume	13	$cm^3 \cdot mol$
F	Faraday's Constant	96485	$C \cdot mol^{-1}$
R	universal Gas Constant	8.314	$J \cdot (mol \cdot K)^{-1}$
T	Temperature	298.15	K
H	Asperity Height	Varied 1–2	μm
c	Standard Deviation	Varied 0.25–1	μm

There have been significant research efforts exploring the use of solid single-ion conducting electrolytes to mitigate and suppress dendrite formation in lithium metal batteries.[1–9] It has been posited that a solid electrolyte with an applied stack pressure could lead to plastic and creep deformation of lithium, limiting dendrite formation and propagation; however, dendrite propagation leading to cell failure has been observed in cells utilizing solid electrolytes.[1,10–14] Several groups have looked at electrochemical-mechanical coupling, particularly the alteration of the thermodynamics and reaction kinetics due to mechanical forces at the electrode/electrolyte interface, and have theorized that electrochemical-mechanical coupling can alter and stabilize the electrode/electrolyte interfacial current distribution. In particular, interfacial regions of high stress become less favorable for plating (which would tend to increase the stress further) and more favorable for stripping (which would tend to relieve the stress).[15,16] The effect of mechanics on thermodynamics can be directly measured by studying the relationship between applied stress and equilibrium potential.[17] However, we are unaware of the measurement of the effect of the interfacial mechanical state of a metal electrode on kinetic transition states during interfacial charge transfer. This measurement involves challenges due to the difficulty of establishing complete contact between two solid surfaces, the need for a well-defined chemical composition at the electrode / electrolyte interface, etc. For these reasons, it is essential to distinguish whether electrochemical-mechanical models for Li plating and stripping are based on mechanical alteration of thermodynamics and/or kinetics, as this influences the facility of model interpretation and experimental validation.

Table I summarizes six prominent models of electrochemical-mechanical coupling and its effects on interfacial current distribution. The first three models are most relevant to the present work and are discussed in greater detail below. The columns in Table I identify the critical aspects of the significant models in this field and should be carefully considered when assessing the applicability and predictions of each model. The analysis column summarizes our view of the model's key focus area(s). The second column indicates how the interfacial stresses are introduced in the model. The Ohm's law in the electrolyte column indicates whether the current distribution in the electrolyte is explicitly solved. The Li mechanical behavior column describes the constitutive model used to model metal electrode mechanics. Solid mechanics (linear elastic, plastic, etc.) are used in some cases, and in others, Li is treated as a viscous fluid. The peak geometry column indicates how the surface roughness, peak, geometry, etc. are defined. Important features of our model in the context of other work in this field include our focus on a secondary current distribution with an experimentally verified electrochemical-mechanical coupling of interfacial thermodynamics, experimentally relevant mechanical initial and boundary conditions to generate the interfacial stress state, both elastic and plastic mechanical behavior for Li metal, and a careful exploration of interfacial geometry through the use of a parameterized Gaussian interface geometry.

In the remainder of this introduction, we discuss several of these papers in more detail to provide rationale and context for the specific choices we make in our model. First, Monroe and Newman studied the role of electrochemical-mechanical coupling for a system with a polymer electrolyte and a metal electrode. They performed a stability analysis based on a mechanics-modified exchange current density.[15,21] In their work, stability was assessed by whether plating was preferential at a Li peak or valley. They first performed a thermodynamic analysis and derived an expression for the change in electrochemical potential of the electron due to pressure changes at the interface for the reaction ($Li \leftrightarrow Li^+ + e^-$):

$$\Delta\mu_{e^-} = F\Delta U = \Omega_{Li}\Delta p_{Li} - \Omega_{Li^+,Elec}\Delta p_{Elec} \quad [1]$$

The electrochemical potential of the electron is directly related to the equilibrium potential of the reaction, U, by Faraday's constant. The authors applied an interfacial force balance to rewrite Eq. 1 in terms of deviatoric stresses, hydrostatic stresses, and surface energy. This expression remains purely thermodynamic:

$$\Delta\mu_{e^-} = F\Delta U = -\frac{1}{2}(\Omega_{Li} + t_-^0\Omega_{LiX}) \times\{-\gamma k + \vec{n}\cdot[\vec{n}\cdot(\Delta\overline{\overline{\tau}}_{Li} - \Delta\overline{\overline{\tau}}_{Elec})]\} + \frac{1}{2}(\Omega_{Li} - t_-^0\Omega_{LiX})(\Delta p_{Li} + \Delta p_{Elec}) \quad [2]$$

In these equations, the partial molar volume of the electrolyte salt, Ω_{LiX}, and the anionic transference number, t_-^0, are estimates from empirical relationships developed from measurements of isothermal diffusion of binary electrolyte solutions (both dilute and concentrated solutions were studied) and do not arise in the derivation of $\Delta\mu_{e^-}$ directly.[22] These terms are used to approximate the value of the molar volume of the lithium cation in the electrolyte, Ω_{LiX}. The applicability of these empirical assumptions (i.e., for Ω_{LiX} and t_-^0) to other electrolyte systems should be carefully considered before use. These estimates may apply to polymer electrolytes using a binary electrolyte; however, they do not apply to inorganic single-ion conductors. Next, Monroe and Newman developed a mechanics-modified Butler-Volmer equation for the electrochemical kinetics at the interface. Here, the thermodynamic expressions are used in a Butler-Volmer transition state analysis to assess how changes in the mechanical state in the electrode and electrolyte affect the kinetic expression. The authors assumed transfer coefficients invariant with the mechanical state in the Butler-Volmer equation and calculated the difference in the transition state height due to changes in the thermodynamic states of the electrode and electrolyte caused by changing pressure. Here, $\alpha_a = \alpha_c = 0.5$, so a single transfer coefficient α is used for simplicity. . The result is a shift in the exchange current density that is given by:

$$i_0 = i_{0,ref}\exp\left(\frac{\alpha\Delta\mu_{e^-}}{RT}\right) \quad [3]$$

Additionally, the surface overpotential, given by $\eta_s = \phi_s - \phi_e - U$, is modified by mechanics as U also shifts due to changes in mechanical state as provided by Eq. 1 above. The Butler-Volmer equation is given by:

Table I. Comparison of prominent Li/electrolyte interface models that include electrochemical-mechanical coupling.

	Model Analysis	Stress generation method	Single-ion conducting electrolyte	Ohm's law in the electrolyte	Li mechanical behavior	Geometry
Our model	Mechanics- Coupled Secondary Current Distribution	Applied Stress	X	X	Elastic-Perfectly Plastic	Gaussian
Monroe[15]	Electrochemical Interfacial Thermodynamic Stability based on Interfacial Mechanics	Interfacial Displacement			Linear Elastic	Sinusoid
Barai 2017[18]	Mechanics-Coupled Exchange Current Density	Contact via applied stress			Linear Elastic	Sinusoid
Barai 2019[4]	Grain Boundary Fracture Stability	Li Deposition creating interface displacement	X	X	Elastic-Plastic with Strain Hardening	Flat
Herbert[19]	Li Metal Deformation Mechanism Map	Li Deposition	X		Creep	Sinusoid
Barroso-Luque[5]	Incipient Crack Fracture Stability	Li Deposition	X		Viscous Fluid Flow	Plating at Semicircle Dendrite Tip
Mistry[20]	Electrodeposition Stability Map	Li Deposition creating interface displacement	X	X	Linear Elastic	Sinusoidal Deformation Field

$$i_{BV} = i_o(e^{\frac{\alpha F \eta_s}{RT}} - e^{-\frac{\alpha F \eta_s}{RT}}) \quad [4]$$

Thus, the interfacial mechanical state modifies the Butler-Volmer equation via both surface overpotential and the exchange current density. Both modifications are based on changing the thermodynamic states of the reactant and product. Future work may also find that an alternative kinetic formulation to the Butler-Volmer equation may be better suited for charge transfer at a Li/solid electrolyte interface.[23]

Using these equations and approaches, Monroe and Newman developed an analytical model for the interfacial current distribution at an interface with a prescribed displacement and a stability criterion for when that current distribution would not lead to further roughening.[3] Although an expression for the current distribution was developed based on interfacial mechanical changes to kinetics and thermodynamics, only variation in the electron electrochemical potential, $\Delta\mu_{e^-}$, a purely thermodynamic quantity, was used in their stability parameter. In addition, their use of a prescribed displacement should be carefully considered: starting from a flat electrode/polymer electrolyte interface without any stack pressure; they applied a sinusoidal displacement at the interface that introduced both tensile and compressive stresses. They considered only linear elastic mechanics and calculated the resultant stresses and their effect on the electron electrochemical potential and the exchange current density. From these calculations, Monroe and Newman indicated an electrolyte with a shear modulus about two times greater than that of lithium should lead to stable plating (i.e., the change in electron electrochemical potential due to interfacial mechanics would lead to preferential plating at Li valleys rather than peaks) for their model parameters. The authors clearly indicate their assumptions and the corresponding model limitations. For example, they highlight how their use of linear elasticity theory limits the model to small strains and neglects Li metal's plastic deformation and creep. Accordingly, their assumption of a prescribed interfacial displacement and only elastic mechanical behavior resulted in maximum stresses in the Li metal and their PEO solid electrolyte of >1 GPa, which is >1000x higher than expected experimentally considering both materials yield at <1 MPa. Additionally, the authors specifically mentioned their neglect of electrolyte fracture, which is now understood to likely be the leading failure mechanism for brittle ceramic electrolytes such as LLZO.[1,14] The assumptions in this model and the use of prescribed displacement for introducing stress at the interface place the model formulation outside expected experimental conditions.

Second, Barai et al. conducted a follow-up work examining the use of the interfacial displacement boundary condition versus a contact boundary condition between a polymer electrolyte and lithium metal electrode.[16] In their work, a flat polymer electrolyte is lowered into a rough metal electrode, modeled with a sinusoidal geometry, until complete contact is achieved. This is an experimentally relevant interfacial mechanical boundary condition, reflecting aspects of cell assembly in a lab. Here, the contact boundary condition results in compressive stresses in the electrode and electrolyte rather than a combination of tensile and compressive stresses in the electrode and electrolyte resulting from a prescribed interfacial displacement of an initially flat interface. The Barai et al. model was a finite-element-method-based computation, and the change in electron electrochemical potential and exchange current density were calculated according to Eqs. 2–4. These simulations indicate that solid electrolytes should always stabilize lithium plating regardless of the electrolyte shear modulus, because higher stresses always occur at peaks in the Li metal, resulting in a lower exchange current density at those peaks during plating.

Barai et al. also studied current focusing and electrolyte fracture in ceramic electrolyte and lithium electrode systems in a model accounting for both kinetics and thermodynamics.[4] A localized model calculates the stress evolution at a grain/grain boundary/lithium interface due to the deposition of a lithium monolayer. Subsequently, they calculated the current densities in the grain boundaries and the grain interiors using the stress-induced change in the electrochemical potential of an electron. In this work, the stress-induced change in the electrochemical potential of an electron was given by:

$$\Delta\mu_{e^-} = F\Delta U = -\frac{1}{2}\Omega_{Li}\{\vec{n}\cdot[\vec{n}\cdot(\Delta\bar{\bar{\tau}}_{Li} - \Delta\bar{\bar{\tau}}_{Elec})]\} + \frac{1}{2}\Omega_{Li}(\Delta p_{Li} + \Delta p_{Elec}) \quad [5]$$

Compared to Eqs. 2, 5 neglects terms containing $t_-^0\Omega_{LiX}$ because lithium ions are a part of the LLZO crystal lattice structure and therefore have a partial molar volume that is not well-defined. However, it should be noted that neglecting $t_-^0\Omega_{LiX}$ in Eq. 1, followed by the procedure used to derive Eq. 2, does not yield Eq. 5; this relates to our comments beneath Eq. 2 on the introduction of t_-^0 and Ω_{LiX}. A derivation supporting this statement can be found in the appendix. Surface curvature terms are also neglected because they examine a flat interface, and these terms are generally of small magnitude relative to the stress terms.

Third, although not included in Table I, Hildebrand et al. derived a mechanics-modified Butler-Volmer equation for a single-ion conductor with a metal electrode, which is the case of specific interest to our model. They found mechanics altered the equilibrium potential according to[24]:

$$\Delta U = \frac{1}{F}(\Omega_M \Delta\sigma_n) \quad [6]$$

They also derived an expression for the mechanics-modified exchange current density, given by:

$$i_o = i_o^{ref}\exp\left(-\frac{\alpha_a \Omega_M \Delta\sigma_n}{RT}\right) \quad [7]$$

It is important to note that Hildebrand et al.'s formulation uses the normal stress rather than the hydrostatic pressure in these expressions. This arises from their derivation focusing on the work required during plating to unidirectionally displace an interface that is under a uniaxial applied mechanical load. In our previous study on Li and Na metal under uniaxial compression, we determined that for high aspect ratios (i.e., with electrode thicknesses substantially smaller than the electrode diameter), yield and plastic deformation in the metals (for stresses large enough for the metal to exceed its Von Mises stress) lead to pressure and normal stress that are nearly identical.[17] We also agree with Hildebrand et al.'s neglect of terms containing $\Omega_{Li^+,Elec}$ for the specific case of a single-ion conducting electrolyte. The implication is that the electrolyte's mechanical state does not affect the thermodynamics at the interface, which we also experimentally observed in our previous work.[17] In the present paper, we follow that earlier work and neglect any influence of the electrolyte mechanical state.

In the present paper, we focus on the effects of the mechanical state at a Li metal / single ion conductor interface on thermodynamics and kinetics and assess the influence of changes in the mechanical state on the interfacial current distribution. We emphasize *quantifying* the impact of stack pressure, interfacial geometry, electrolyte ionic conductivity, and exchange current density on the current distribution. This work focuses on how (1) experimentally relevant mechanical boundary and initial conditions and (2) interfacial geometry affect the current distribution. Regarding (1), we start with a stress-free initial condition and apply a uniaxial stack pressure, which is experimentally relevant. Regarding (2), while in previous studies a sinusoidal peak was used to define the interfacial geometry, here we study how the interfacial geometry, particularly

height, protrusion direction (e.g., Li peak vs Li valley), and tip curvature, impact current focusing based on a secondary current distribution with various electrolyte ionic conductivities. In this work, as stated in Table I, we are modeling a mechanics-coupled secondary current distribution but are not predicting dendrite or void formation. However, the model formulation does apply to both plating and stripping.

Methods

We conducted simulations using the finite element analysis software COMSOL Multiphysics and the Structural Mechanics and Electric Currents packages, and our modeling domain and select equations are shown in Fig. 1. We developed an electrochemical-mechanical model for a lithium metal anode in contact with a solid-state electrolyte with the mechanical properties of the ceramic electrolyte LLZO. This secondary current distribution model applies to both plating and stripping; however, we primarily show modeling results for the case of plating. We swept the electrolyte ionic conductivity to quantify the impacts of both ionic transport and kinetic limitations. We chose to study two applied current densities to reflect a slow and a fast charge scenario and two values of interfacial area-specific resistance (ASR) to reflect a low resistance (1 ohm-cm^2 at 1 mA cm^{-2}) heat-treated interface based on literature and a higher resistance interface (10 ohm-cm^2 at 1 mA cm^{-2}).[2,3] We treated the electrolyte as a linear elastic material, which is appropriate for LLZO. We treated the Li metal electrode as linear elastic followed by perfectly plastic mechanical behavior once the Von Mises stress exceeded the yield strength (0.7 MPa at 25 °C) and made this choice due to Li's lack of work hardening at low strain rates and room temperature. The Von Mises yield criterion requires the second invariant of the deviatoric stress to reach a critical value, the yield strength, before plastic deformation occurs. Confined walls limit the formation of shear stresses; however, Poisson's ratio for Li leads to unequal principal stresses, creating deviatoric stresses. For the case of negligible shear stresses, the Von Mises yield criterion is given by the equation:

$$\sigma_v = \sqrt{\frac{1}{2}[(\sigma_{xx} - \sigma_{yy})^2 + (\sigma_{yy} - \sigma_{zz})^2 + (\sigma_{zz} - \sigma_{xx})^2]} \quad [8]$$

As shown in Fig. 1, the model is 2D, and we use a plane strain assumption. At the left and right boundaries, we constrain displacement in the x-direction. The top boundary of the electrolyte has an applied load to simulate a stack pressure, and we constrain the bottom lithium boundary in the x- and y-directions. We use a Gaussian function to the electrode / electrolyte interface to simulate a geometric region such as a protruding ("Lithium valley") or missing ("Lithium peak") solid electrolyte grain, as observed experimentally in Fig. 1A:

$$y = H \exp\left(-\frac{(x-5)^2}{2c^2}\right) \quad [9]$$

The value H controls the height and c controls the width of the interfacial roughness. A negative value of H results in a Li valley, and a positive value results in a Li peak. We then assess the impact of this geometric region through the current distribution along the entire interface. The amplitude of the Gaussian function is varied to evaluate the effect of protrusion dimensions on the current distribution; the amplitude magnitudes are at the micron scale to reflect the

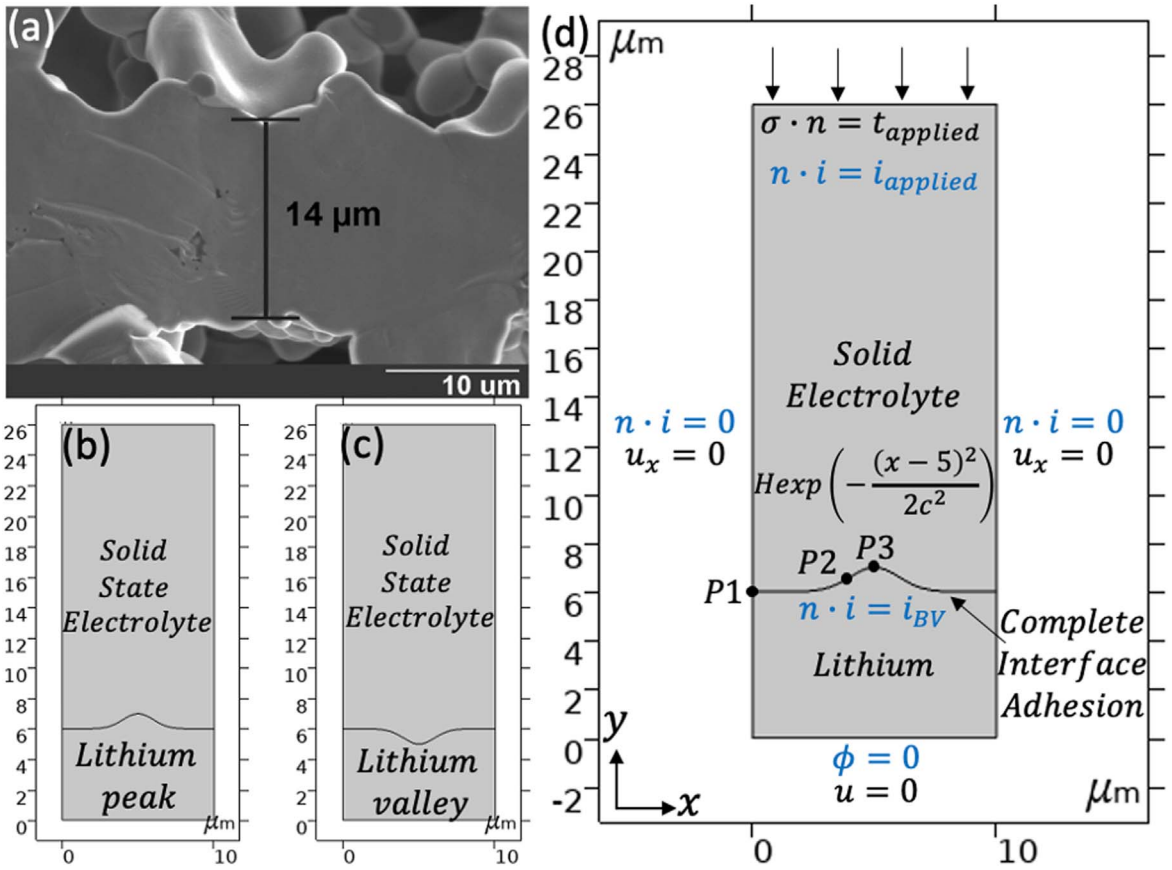

Figure 1. (a) SEM image of dense LLZO layer reproduced from Hitz et al.,[3] which serves as an example of the geometry at a Li/solid electrolyte interface (b) Example of Lithium Peak in our model. (c) Example of Lithium Valley in our model. (d) Modeling domain with boundary conditions. Mechanical boundary conditions are denoted in black text, and electrochemical boundary conditions are denoted in blue text. The Gaussian function indicates the protrusion geometry at the electrode/electrolyte interface. P1, P2, and P3 are points for comparing stresses and current densities.

observations of interface geometry in sintered ceramic separator samples, with an example cross-section included in Fig. 1A.[3]

Our mechanical boundary conditions differ from those employed by both the Monroe and Barai works. We start with a stress-free, rough electrode / electrolyte interface. A rough interface can arise after experimental processing involving compression (to achieve partial contact) and heat treatment near the melting temperature of Li (to achieve complete contact and stress relaxation[6,25–27]; the resulting interface roughness simply reflects the solid electrolyte, with both peaks and valleys. We use an interfacial mechanical condition that practically corresponds to complete adhesion between the Li metal electrode and the LLZO solid electrolyte at their interface. Mathematically, this means that at node points along the interface, stresses and displacements are equivalent in the electrode and electrolyte. To this stress-free interface in complete contact, we then apply a stack pressure and find the resultant mechanical conditions in the electrode and electrolyte. The stack pressure introduces compressive stresses. Electrolyte roughness protruding toward the electrolyte bulk (referred to as a Li peak here) causes decreased stress at the Li peak for a given stack pressure, whereas electrolyte roughness protruding toward the Li bulk (referred to as a valley here) leads to increased stress at the Li valley.

The current density for deposition of Li at the electrolyte/Li interface is described using the Butler-Volmer equation given in Eq. 4. The overpotential with modification due to mechanical stresses is given by the equation:

$$\eta_s = \phi_1 - \phi_2 - U \qquad [10]$$

Here, the equilibrium potential, U, is a function of the mechanical state as given in Eq. 5. Our previous experimental work indicates that the mechanical state of the electrolyte has no impact on the thermodynamics of the electrochemical reaction; thus, it does not appear in Eq. 6.[17] Equation 10 differs from Eq. 6 due to the use of hydrostatic stress (pressure) rather than the normal stress in the calculation of U (see below). We note that the use of pressure, rather than normal stress or a strain energy term, in the thermodynamic formulation of stress-potential coupling may benefit from further analysis. However, in the case of Li metal, because of its low yield strength and the mechanical boundary conditions, the magnitude of deviatoric stresses is limited, and the hydrostatic pressure should describe the mechanical state well.

Equation 11 gives the change in electrochemical potential within the Li metal due to a change in pressure:

$$\Delta\mu_{e^-} = F\Delta U = -\Omega_{Li}\Delta p_{Li}. \qquad [11]$$

Equations 10 and 11 are inserted into Eqs. 3 and 4 to calculate the current density at the interface.

We apply a uniform normal current distribution to the top electrolyte boundary. Ohm's law is solved in the electrolyte and electrode bulk. The lithium bottom boundary is set to a potential of 0 V. The electrolyte's and electrode's right and left boundaries are treated as insulating. These boundary conditions simulate plating. Changing the direction of the applied current distribution at the top boundary would simulate stripping. For primary and secondary current distributions without coupling to mechanical state, plating and stripping current distributions are symmetric, i.e., exactly equal in magnitude along the interface, with opposite sign. When the mechanical state along the interface is included, it will affect plating and stripping current densities in different ways and result in non-symmetric plating and stripping current distributions. In the Results and Discussion section, all results are for the plating case, aside from Fig. 5 which provides a comparison between plating and stripping.

The present model has several limitations. (1) The model is stationary and considers only a single point in time at the start of deposition or stripping. Thus deposition-induced stresses (i.e., stresses caused by plating Li at the interface) or stripping-induced stress relaxation, as well as stress relaxation via creep, are not considered. Deposition-induced stresses will be of the largest magnitude at locations experiencing the highest current density, which may be a function of time (2). While here we treat Li as elastic-perfectly plastic, Li metal demonstrates creep at operating conditions relevant to commercial applications. Creep would serve as a stress relaxation mechanism, reducing stress gradients. Li is not a perfectly plastic material and has been demonstrated to exhibit different mechanical properties depending on sample aspect ratio, compression versus tension, and even sample size.[28–30] (3) We assume an isotropic electrolyte without surface or bulk heterogeneity. Ceramic electrolyte separators are polycrystalline, with grain boundaries that may have different ionic conductivity and mechanical properties than the bulk.[31] Grain orientation may also impact the current distribution at the micron to 10 s of micron-scale in our model. (4) The model does not consider electrolyte fracture initiation and propagation. In the event of significant stresses at the crack tip, the stress intensity factor may exceed the fracture toughness of the electrolyte and cause crack initiation and propagation. More generally, the most physically accurate model is transient and calculates stress and electrochemistry evolution as Li is plated or stripped. Because our model is stationary, the effect of cycling-induced stresses/relaxation is absent. The geometric effects on the current distribution will remain in a transient model; however, they may change over time due to uneven deposition or stripping. In the case of dendrite formation during plating, dendrite propagation can introduce new surface area for charge transfer. For stripping, void formation can occur, eliminating surface area for charge transfer. Additionally, a transient model could capture the effect of stress relaxation via creep deformation and electrolyte fracture. Our model captures the current distribution at a single point in time of a mechanically stress-free, as-fabricated solid-state cell; the discussion in the context of Fig. 7 below qualitatively describes the implications of our model for transient operation.

Results and Discussion

Figures 2 and 3 depict the developed pressures (i.e., hydrostatic stresses) for two boundary loads. Figure 2 demonstrates the Li peak case. An applied stress of 1 MPa, indicative of the approximate upper limit for stack pressure on an automotive cell, does not cause large enough Von Mises stresses to cause plastic deformation of Li. Additionally, the interfacial pressure is higher at P1 than P3, indicating that mechanics modification to the Butler-Volmer equation would favor enhanced deposition at the tip. The pressure is lowest at a Li peak and highest at a Li valley due to the uniaxial load boundary condition, the protrusion geometry, Poisson's ratio in the domains, and our use of a complete mechanical adhesion at the interface. We emphasize that the mechanical conditions at the Li metal / solid electrolyte interface are critical for the analysis of the resulting mechanics-coupled current distribution along the interface. Assuming complete adhesion between the Li metal and solid electrolyte (as we do here) gives the opposite result compared to a contact model including a frictionless interface (as done in ref 9), in terms of whether the pressure at P3 is larger or smaller than P1. At an applied load of 10 MPa, plastic deformation occurs everywhere within the Li due to the Von Mises stresses exceeding that of the yield criterion, limiting stress variations within the Li along the interface. For example, for the 1 MPa applied load, there is a difference of ~0.2 MPa along the interface (~25%), while for the 10 MPa case, there is a difference of ~0.25 MPa (~2.5%).

The results observed here differ from those indicated by Barai et al., reinforcing the importance of mechanical boundary and initial conditions. Because Barai et al.'s boundary and initial condition resulted in higher stresses at the peak tip, they observed a lower current density at Li peaks than valleys. However, we would expect a transient version of our model to also result in a higher stress at P3 than P1 due to deposition-induced stress rise at that point. However, as discussed below, the magnitude of variations in the mechanical state along a rough interface that is calculated here has a limited

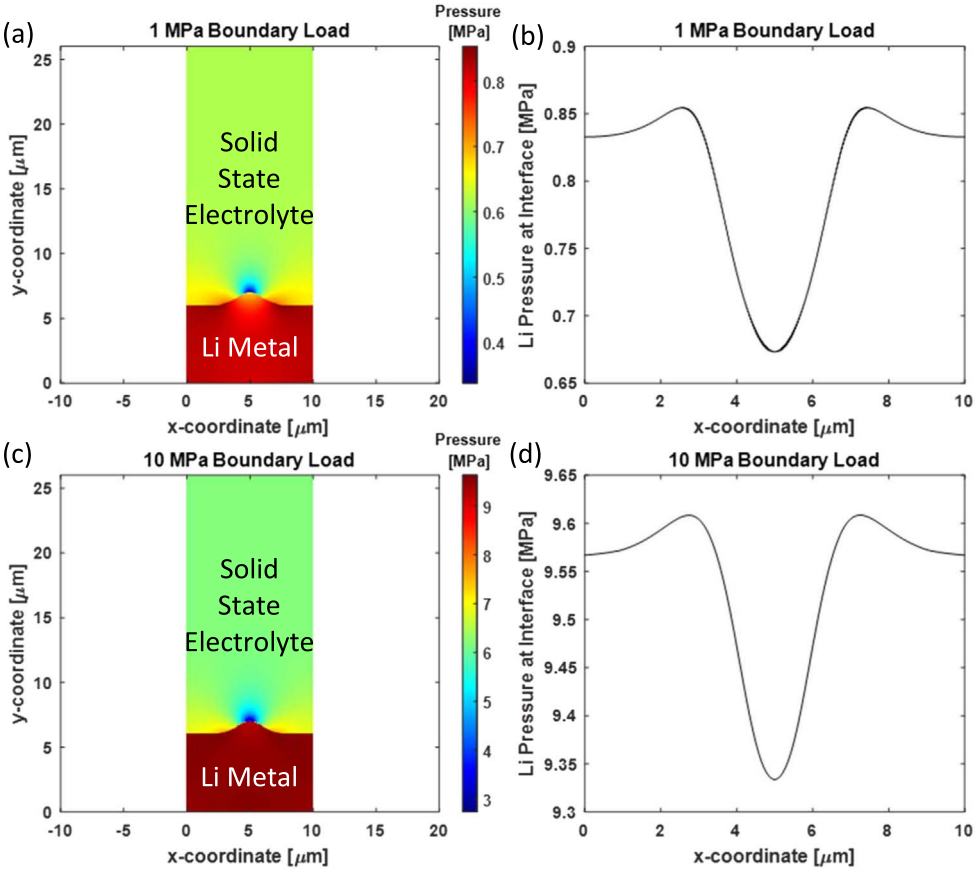

Figure 2. Pressure and Li interfacial pressure diagrams for a Li peak. (a) Pressure for an applied stack pressure of 1 MPa. (b) Interfacial pressure in the Li electrode for an applied stack pressure of 1 MPa. (c) Pressure for an applied stack pressure of 10 MPa. (d) Interfacial pressure in the Li electrode for an applied stack pressure of 10 MPa. A Li peak with Gaussian parameters h = 1 μm and c = 1 is used for all panels shown.

impact on the current distribution because the magnitude of stress variations along the interface is too small to result in a significant variation in either thermodynamic potential or exchange current density.

Figure 3 demonstrates the case of a Li valley. As shown previously, a boundary load of 1 MPa is insufficient to cause plastic deformation of the Li electrode. With a boundary load of 10 MPa, the Von Mises stress is exceeded everywhere in the Li domain, and plastic deformation occurs. In this case, the stresses are largest at P3, which would reduce the plating and increase the stripping current density according to Eqs. 4, 6, and 7.

Applied loads exceeding a material's yield strength do not necessarily indicate that plastic deformation will occur; for example, the boundary conditions and aspect ratio affect the stress tensor within the material, from which yield can be estimated. For example, an applied load of 1 MPa, greater than the yield strength of Li (~0.7 MPa at 25 °C), does not cause plastic deformation. Plastic deformation, when it occurs, is crucial because it mitigates the formation of stress variations along the interface of the Li electrode and a SIC electrolyte, minimizing the effect of mechanics on current density variations. In cases where plastic deformation does not occur, the generated stresses are not large enough to significantly impact electrochemistry. Based on Eq. 5, to shift the equilibrium potential of Li by 1 mV, a pressure difference of ~7.4 MPa is required. The difference between the maximum and minimum stresses observed in Fig. 1 would only shift the value of the equilibrium potential by a fraction of 1 mV. *These results demonstrate that stresses generated by the stack pressure alone have a negligible impact on interfacial electrochemistry*. Additionally, deformation via creep has been exhibited in conditions relevant to battery operation (e.g., temperature, strain rates), serving as another means of stress relaxation and further limiting stress gradients.[30,32] Stress differences on the order of 100 s of MPa would alter the equilibrium potential by 10 s of mV and could strongly influence the current distribution, but in our view, the only likely practical situation in which such large stress variations could occur is in the context of a crack, where the rate of Li deposition exceeds that of the flow of Li from the crack into the electrode bulk.[5] This mechanism was not considered in the present model but will be considered in future work.

To directly quantify the role of interfacial pressure variations on the current distribution in the context of other key variables that influence the current distribution (e.g., the electrolyte ionic conductivity and the reference exchange current density), Fig. 4 shows the ratio of the plating current density at P3 and P1 as a function of the electrolyte ionic conductivity for three cases: (1) the Butler-Volmer equation unaffected by mechanics, (2) the Butler-Volmer equation with a mechanically altered exchange current density, and (3) the Butler-Volmer equation with a mechanically altered exchange current density *and* a mechanically altered equilibrium potential. A ratio greater than 1 indicates a larger magnitude current density at P3 (i.e., a higher rate of deposition or stripping). This figure demonstrates the importance of including Ohm's law in the electrolyte and directly quantifies the limited effect of electrochemical-mechanical coupling on the current distribution. In all four cases, increasing the ionic conductivity to increase the ratio of kinetic to transport resistance leads to P3:P1 ratios approaching unity, which indicates a more uniform current distribution. In panel A, we observe mechanics does have an effect as the current density P3:P1 ratio is higher for $\kappa > \sim 10^{-5}$ $\cdot cm^{-1}$ with mechanics included vs without. This small effect stems from smaller stress at P3 compared to P1, as demonstrated in Fig. 1. The smaller stress makes

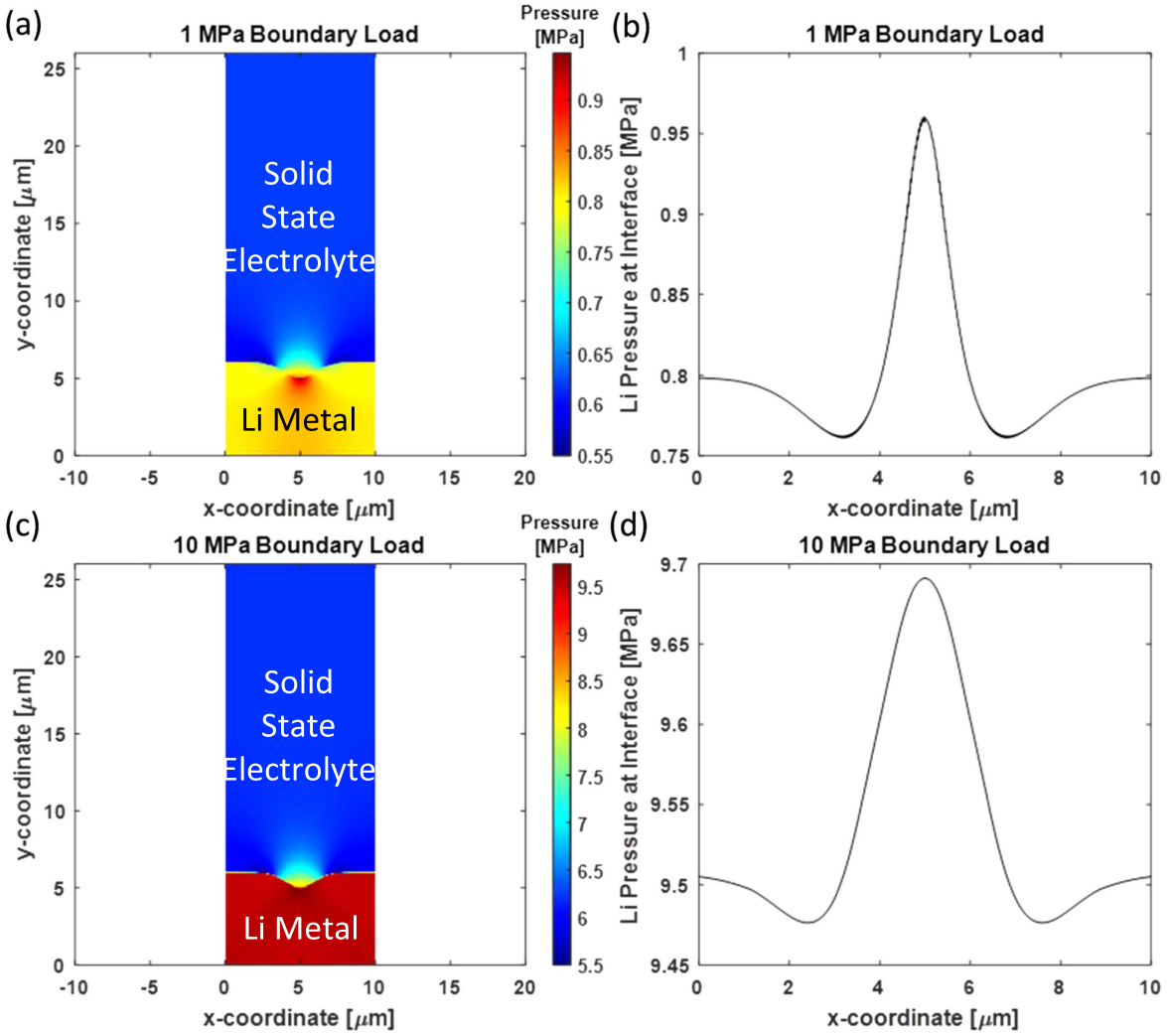

Figure 3. Pressure and Li interfacial pressure diagrams for a Li valley. (a) Pressure for an applied stack pressure of 1 MPa. (b) Interfacial pressure in the Li electrode for an applied stack pressure of 1 MPa. (c) Pressure for an applied stack pressure of 10 MPa. (d) Interfacial pressure in the Li electrode for an applied stack pressure of 10 MPa. A Li valley with Gaussian parameters h = 1 μm and c = 1 is used for all panels shown.

plating at P3 more favorable when mechanics are included due to Eqs. 5 and 8. The higher P3:P1 current density ratio with mechanics included is only observed in Fig. 4a. To observe mechanics-modification of the current distribution for small interfacial stress variations, as seen in panel 4a, two criteria need to be present: (1) a small magnitude of η_s is required (which is achieved through a small current density and/or a small kinetic resistance), and (2) the current distribution needs to be influenced by the interface kinetics (i.e., the current distribution should not be principally determined by the electrolyte ohmic resistance alone). In panel 4a, criteria (1) is met for all values of κ, but the impact of mechanics on i_{P3}/i_{P1} is greater for high κ because of criteria (2). In panels 4b to 4d, the magnitude of η_s is greater than in panel 4a due to either a higher kinetic resistance (panels 4c and 4d) and/or a higher current density (panels 4b and 4d), masking the effect of the fixed change in $\Delta\mu_{e^-}$ from mechanics uniformly present in all panels of Fig. 4.

Figure 5 illustrates the impact of electrochemical-mechanical coupling on the current distribution for plating vs stripping for two geometries, a broad Li peak (left column) and a sharp Li peak (right column), for the case where the asymmetry is the greatest (i.e., at 1 mA·cm^{-2} and 1 Ω·cm^2). Here, we highlight that the effect of mechanics on the current distribution (panels i, j) is not symmetric for the cases of plating and stripping, and that asperity geometry influences the extent of asymmetry. Figures 5a and b show that the interfacial pressure in the Li electrode is exactly the same for both plating and stripping regardless of the geometry; this is set by the imposed stress and mechanical boundary conditions. Note, that our static model does not account for stress changes during transient plating or stripping. Arising from the equivalent stress profiles, the mechanics-modified exchange current density (Figs. 5c and d) and equilibrium potential (Figs. 5e and f) are also identical for plating and stripping. However, the surface overpotential is different for stripping and plating (Figs. 5g and h). In 5 g and 5 h, $-\eta_{s,plate}$ is plotted to allow direct comparison with $+\eta_{s,strip}$. If electrochemical-mechanical coupling is not included, the values of these two terms would be identical. The lack of symmetry in the surface overpotentials leads to a lack of symmetry in the electrode normal current density (Figs. 5i and j). In 5i and 5j, $+i_{BV,plate}$ and $-i_{BV,strip}$ are plotted to allow direct comparison of the magnitudes. The small magnitude of interfacial stress variations in pressure observed in panel 5a with the broad Li peak geometry results in the ∼5% maximum difference in current density between plating and stripping seen in panel 5i. However, increasing asperity height and sharpness results in a larger interfacial variation in pressure seen in panel 5b, which results in the ∼10% maximum difference in current density between plating and stripping seen in panel 5j. As shown in panels 5e and 5 f, the interfacial pressure distribution results in a 0.02 mV (panel 5e) to 0.08 mV (panel 5 f) variation in U; these small variations will impact the current distribution when the magnitude of η_s itself is small, as seen in panels 5 g and 5 h. However, as

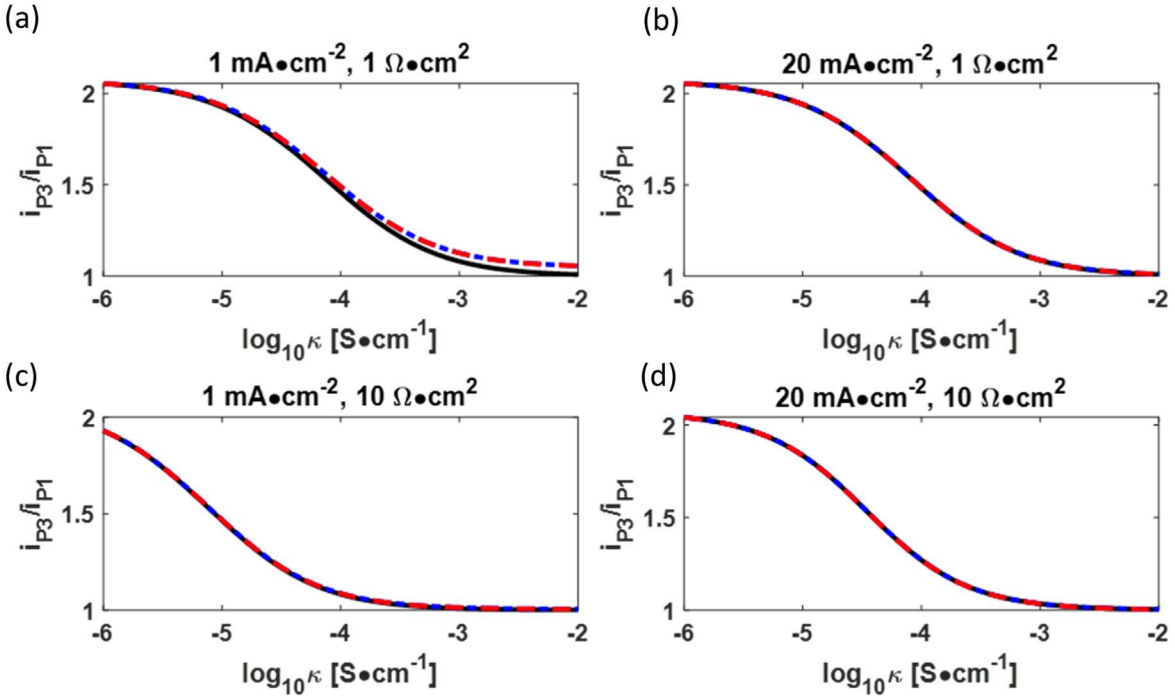

Figure 4. Effect of ionic conductivity on plating current density at peak and valley for the geometry shown in Fig. 1 above. A 1 MPa boundary load was used for all cases. The applied current density was set to 1 mA·cm^{-2} (a) and (c) or 20 mA·cm^{-2} (b) and (d). The exchange current density was set to provide an ASR of 1 (a) and (b) or 10 Ω·cm^2 (c) and (d) based on an applied current density of 1 mA·cm^{-2}. P3 and P1 locations are shown in Fig. 1.

demonstrated in Fig. S1, a higher applied current density increases the magnitude of η_s and overrides the small effects of mechanics on η_s, resulting in a ∼1% maximum difference in current density between plating and stripping. In contrast, Fig. S2 demonstrates that a smaller applied current density decreases the magnitude of η_s and increases the effects of mechanics on η_s, resulting in a ∼30% difference in current density between plating and stripping.

Figure 6 demonstrates the effects of asperity geometry and electrolyte ionic conductivity on the P3:P1 plating current density ratio. A fully modified Butler-Volmer equation was used (Eqs. 4, 10, 11) for Fig. 6. Panels 6c and 6d show the domain pressure and interfacial pressure in the Li electrode for the most extreme cases, 2 μm asperities with c = 0.25. For these cases, the maximum stress variations along the interface are <1 MPa, corresponding to a <1 mV change in the equilibrium potential of Li. It can be observed that both the height and width of the peak play essential roles in the current distribution. As the peak width decreases, the tip's curvature increases. Previous studies have not carefully examined the role of this interfacial geometry (e.g., peak shape, tip curvature, inter-electrode spacing). Figure 6A shows the P3:P1, and Fig. 6b shows the P3:P2 current density ratios. For low ionic conductivity electrolytes, a primary current distribution is approached, and the current distribution is sensitive to both the peak height and the width. Due to geometric effects, current shielding can occur on the edges of the peak, as observed by comparing Figs. 6a and b. At an ionic conductivity of 10^{-6} S·cm^{-1}, the current density at P2 is ∼5x smaller than at P1. As the ionic conductivity increases and kinetic resistance becomes a factor, current focusing becomes more sensitive to the peak height rather than its width and curvature. At high ionic conductivities (>10^{-3} S·cm^{-1}), kinetic resistance dominates, and the current distribution becomes more uniform; however, the current distribution at P3 remains 5%–10% greater (due to geometric factors) than those observed at P1 or P2.

Figure 7 depicts the same conditions as in Fig. 6, except for a Li valley rather than a peak. Figure 7a shows P3:P1 current density ratio, and Fig. 7b shows the ratio for P3:P2. As observed in Fig. 6, ohmic resistance determines the current distribution at low ionic conductivity values. As the ionic conductivity increases, the current density ratios do not converge to a value near unity, as observed in the previous case. In addition, as the ionic conductivity falls, the P3:P1 and P3:P2 ratios both approach 0. With all else equal between Figs. 6 and 7, the significant difference in the current distributions is due to geometric effects. We emphasize that this asymmetry caused by geometric effects alone has not been identified and discussed in previous models of a Li metal / solid electrolyte interface and can have important implications for interface evolution, as described in the following section. An experimental implication of Fig. 7 is that a solid electrolyte / lithium metal interface that is flat, and in particular one that avoids high-curvature peaks or valleys, should result in a more uniform current density and potentially the ability to cycle at higher rates and areal capacities without impedance rise or failure. Indeed, the observation that the solid electrolyte LiPON can cycle Li metal with stable performance with a low ionic conductivity value (∼10^{-6} S·cm^{-1}) has been attributed by some to the absence of the grain boundaries present in polycrystalline ceramics and some glasses.[26,33,34] Our analysis here presents a novel possible reason for this observation with LiPON; namely, the deposition of LiPON results in a flat interface that avoids a high-curvature interfacial geometry that is more likely to result from grain-based separator structures.

Effect of non-uniform current distribution on interfacial evolution.—The present analysis indicates that non-uniform current densities will result primarily from geometric considerations for Li peaks and valleys. Figure 8 demonstrates the current and potential distributions for a rough Li/electrolyte boundary and includes an illustration depicting the possible transient implications for the cases of both plating and stripping. These illustrations assume perfect initial interfacial contact, isotropic electrolyte and electrode properties, and an interface free of spatial variations in kinetics and other properties. Figure 8a shows stripping at a lithium valley and peak. Here, geometric effects cause a minimal stripping rate at the valley bottom and a maximum stripping rate at the peak tip. In these cases, if the mechanical flow of lithium cannot resupply lithium to the interface to match the stripping rate, void formation can occur at both the Li valley and peak. For the valley, the valley walls could be

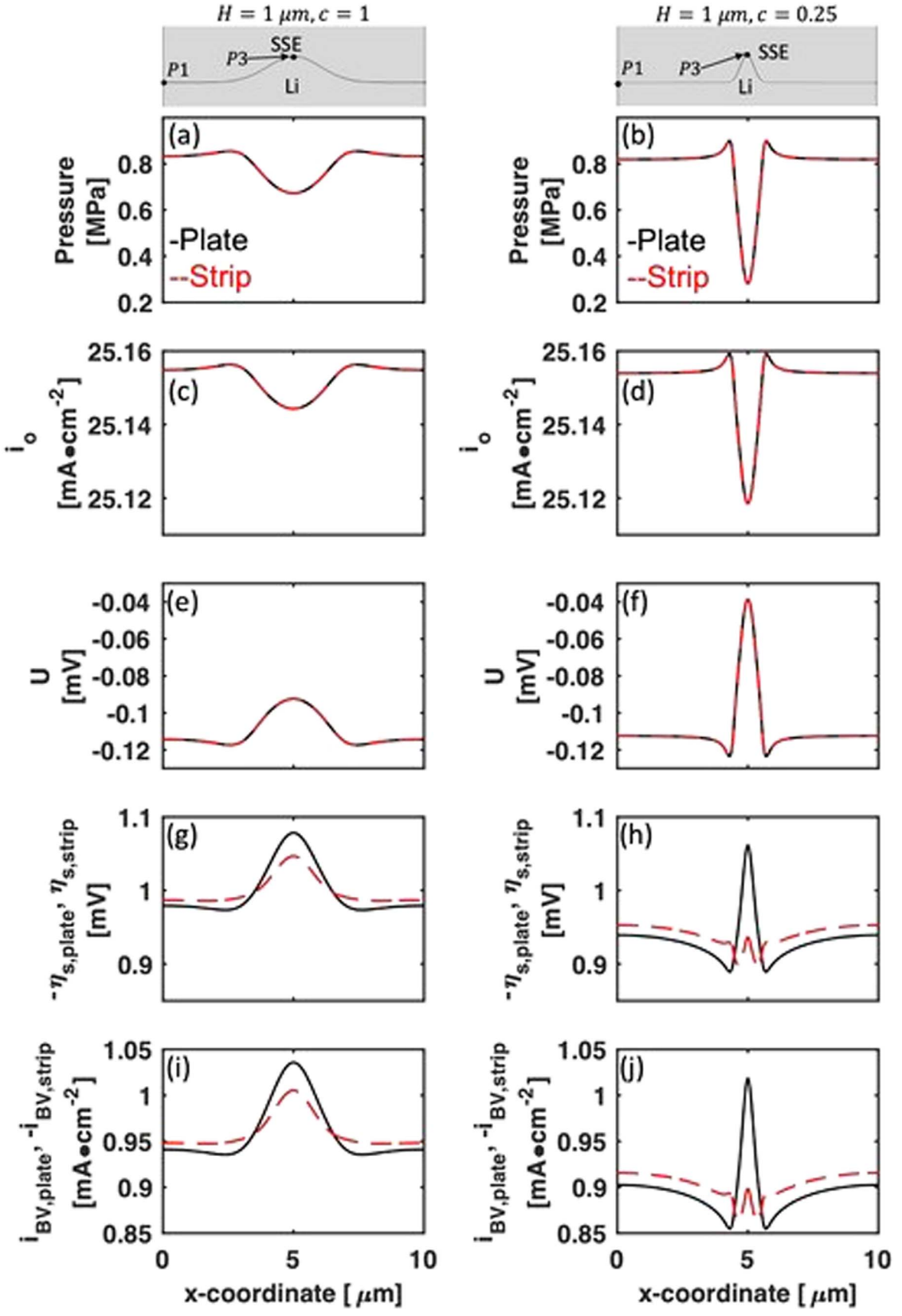

Figure 5. Electrochemical-Mechanical Couplings as a function of electrode x-coordinate for Stripping and Plating. The left column has results for a Li peak with H = 1 μm and c = 1, and the right column has results for a Li peak with H = 1 μm and c = 0.25. (a) and (b) Interfacial pressure in the Li electrode. (c) and (d) mechanics-modified exchange current density. (e) and (f) Mechanics-modified equilibrium potential. (g) and (h) Surface overpotential (note the signs). (i) and (j) Electrode interfacial current density (note the signs). For all cases, the exchange current density is for an ASR of 1 Ω•cm^2 at 1 mA•cm^{-2}, an applied current density of 1 mA•cm^{-2}, κ = 1 mS·cm^{-1}, and an applied boundary load of 1 MPa.

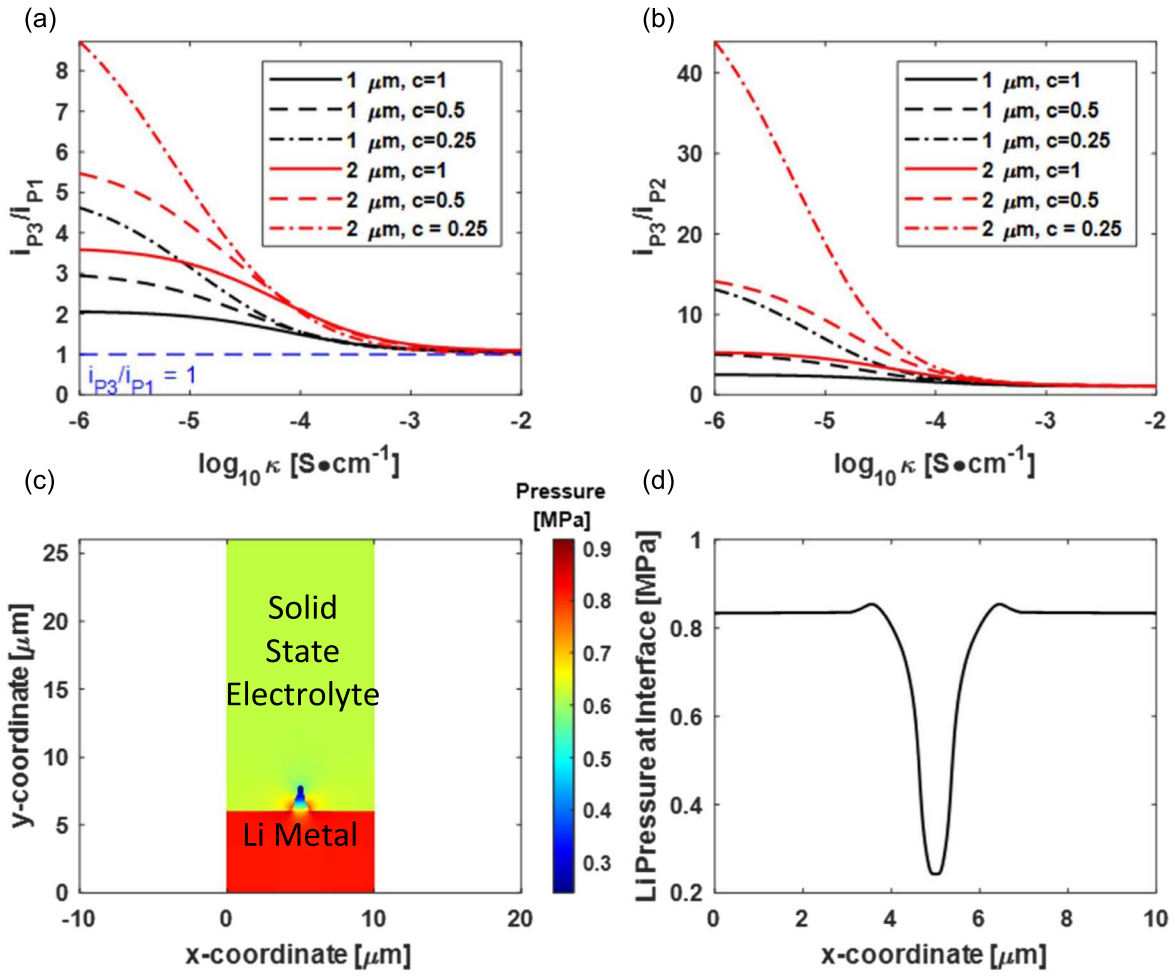

Figure 6. Effect of peak geometry on plating current density ratio for a Lithium Peak. (a) The P3: P1 current density ratio. (b) The P3:P2 current density ratio. (c) Pressure at an applied stack pressure of 1 MPa for an asperity with H = 2 μm and c = 0.25. (d) Interfacial pressure in the Li electrode for an asperity with H = 2 μm and c = 0.25. For all cases, the exchange current density is for an ASR of 1 Ω•cm^2 at 1 mA•cm^{-2}, and an applied current density of 1 mA•cm^{-2} is used. H indicates the peak height (1 or 2 microns), while the parameter c describes the peak width (larger is wider); see Eq. 9.

stripped faster than the valley bottom, leading to void formation along the wall. At the Li peak, the high stripping rate could cause void formation at the tip. If stripping continues for long times past t_2, Li may be restored to the interface eliminating the formed voids; however, if plating occurs before the voids are eliminated, the voids may become occluded (i.e., voids within the bulk Li). Void formation on stripping has been observed and discussed by several authors.[35–38] Still, careful consideration of the role of interfacial geometry (e.g., Li peaks vs valleys) is not typically included. Next, we depict plating at a lithium valley and peak in Fig. 8b. For the lithium valley, the current density is at a minimum at the bottom, and for the peak, the current density is at a maximum at the tip, both due to geometric effects. After sustained plating, the unequal deposition rates are expected to affect the interface. At the valley, sustained higher plating rates at the top of the valley could cause delamination and the formation of a void at the base of the valley as deposited lithium pushes the lithium away from the solid electrolyte. In other words, this is a mechanism for void formation on plating, which has not previously been discussed. At the Li peak, the higher deposition rates at the tip could lead to metal accumulation at the peak. If this exceeds the deposition rate on the walls, delamination of Li metal from the solid electrolyte could occur, again leading to a void. Delamination assumes no fracture of the electrolyte preventing the growth of the dendrite and that Li metal does not deform in the in-plane direction from regions of high deposition rate to low deposition rate. The present study does not account for deposition or stripping-induced stresses, which may lead to large stress gradients between the asperity tip and electrode bulk. These stress gradients may be large enough to shift the current distribution but can also lead to electrolyte fracture and crack propagation. In both cases, delamination and void formation lead to electrochemically inaccessible areas for further deposition. Continued deposition could increase the size of the formed voids. It should be noted that stripping/plating for very long times or pulse cycling behavior could result in different surface morphologies. Void formation and delamination are expected to depend on stack pressure and the properties of the Li metal, which are functions of temperature. To summarize, the transient implications of our current distribution model indicate several novel and critical points for consideration, including that (1) on stripping, void formation at a Li valley vs a Li peak may occur in different ways involving the current distribution and Li metal movement, and (2) that on plating, void formation may also be possible, including at both Li peaks and valleys.

Conclusions

For single-ion conductor / lithium metal systems, the thermodynamics and kinetics of metal plating and stripping can be altered by the mechanical state of the lithium metal. The major findings of this paper include: (1) The mechanical state of a single ion conductor does not affect the electrochemical kinetics. It is essential to start from the original equilibrium equations if developing an equation that considers the mechanical state of the electrolyte (appendix). (2) The mechanical initial and

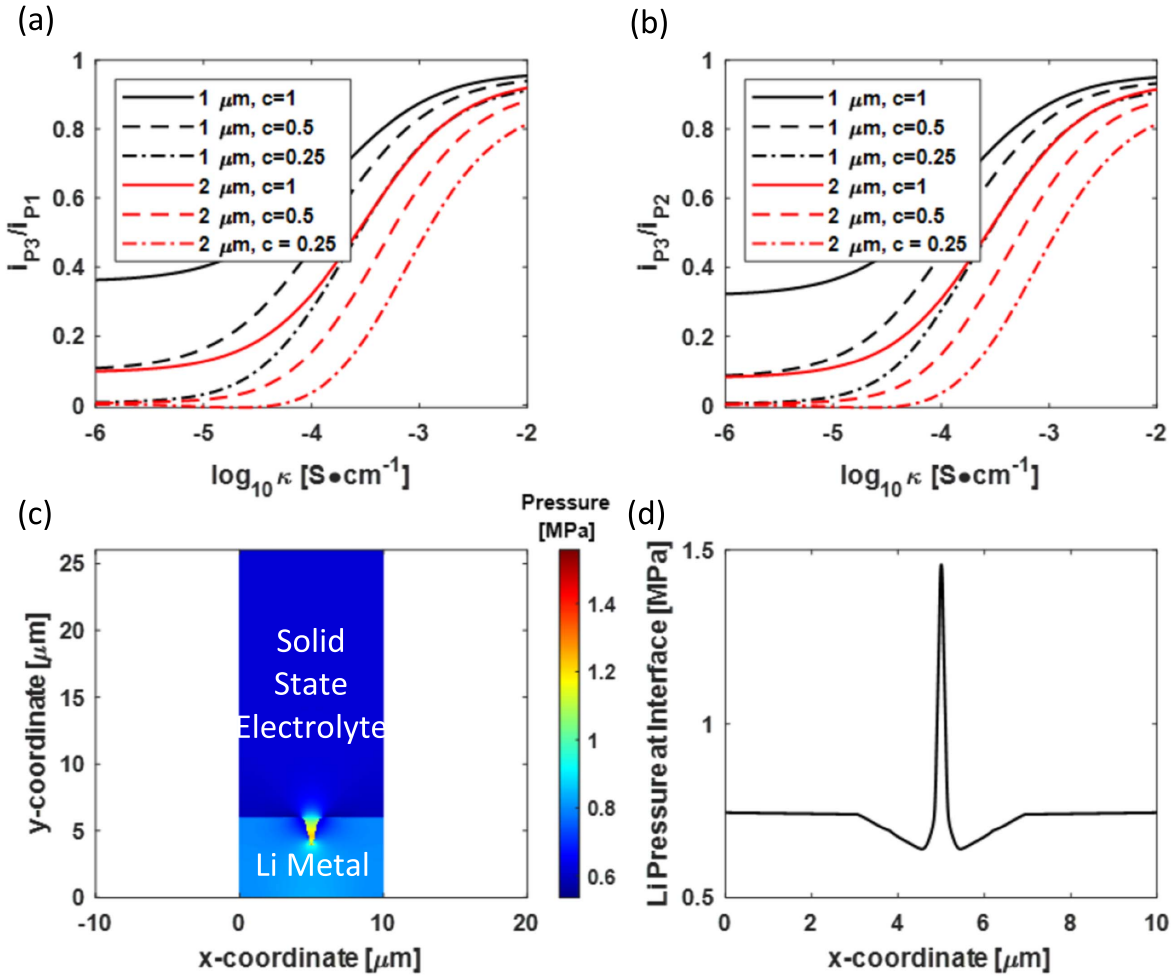

Figure 7. Effect of protrusion geometry on plating current density ratio for a Lithium valley, with all other conditions the same as in Fig. 6. (a) The P3:P1 current density ratio. (b) The P3:P2 current density ratio. (c) Pressure at an applied stack pressure of 1 MPa for an asperity with H = 2 μm and c = 0.25. (d) Interfacial pressure in the Li electrode for an asperity with H = 2 μm and c = 0.25. For all cases, the exchange current density is for an ASR of 1 Ω•cm^2 at 1 mA•cm^{-2}, and an applied current density of 1 mA•cm^{-2} is used. H indicates the peak height (1 or 2 microns), while the parameter c describes the peak width (larger is wider); see Eq. 9.

boundary conditions and the mechanical constitutive model significantly affect model predictions of mechanical state at a lithium metal / solid electrolyte interface. For considerable stack pressures (e.g., 10 MPa), plastic deformation limits stress variations, preventing variations in the mechanical state along the rough interface from significantly altering the current distribution (for a purely linear elastic model, stress gradients would continue to increase). (3) The mechanical variations along a rough interface with experimentally relevant electrochemical and mechanical initial and boundary conditions *are not* expected to influence the current distribution in a quantitatively significant way (i.e., by >10%), and geometric effects associated with Ohm's law are expected to be more important than mechanical effects. In other words, for typical surface roughness expected on a non-polished solid electrolyte separator, mechanical stress variations along that interface will not make the current distribution (and hence the distribution of plating or stripping) significantly more or less uniform. For example, for practical stack pressures (e.g., 1 MPa), pressure gradients along the interface lead to sub-mV changes in the equilibrium potential, which results in minor effects on the current distribution (i.e., a few percent at most due to mechanics alone). (4) The effects of electrochemical-mechanical coupling are not symmetric for plating and stripping. For a given geometry and interfacial stress distribution, the exchange current density and equilibrium potential are modified equally for plating and stripping; however, the magnitude of the surface overpotential, and interfacial current distribution demonstrate asymmetry. This effect is enhanced for higher and sharper asperities due to a higher variation in interfacial stress. We emphasize that while mechanics has a ~1% effect on the current distribution along an interface for either plating *or* stripping, the impact can be ~10% for plating vs stripping. The asymmetry between plating and stripping is most evident when the magnitude of η_s is small (i.e., when the small magnitude of ΔU due to mechanics can impact η_s), and when the current distribution is influenced by the interface kinetics (i.e. when it is not principally determined by ohm's law in the separator). (5) The current distribution effects associated with peaks vs valleys are not symmetric, largely due to geometry aspects of Ohm's law. In other words, the current distribution around a peak and valley with the same width and height may significantly differ. These effects were studied for several asperity geometries and directions, and geometric effects were found to have more influence on the current distribution than mechanical effects. (6) This analysis is not a stability assessment for dendrite initiation and propagation. However, we include a discussion and schematic of how continued non-uniform plating *or* stripping could lead to void formation or delamination of the Li/electrolyte interface, including for both Li peaks and valleys. The potential for void formation on plating has not been previously described and may benefit from experimental investigation. More generally, this work indicates that increasing experimental attention to interfacial geometry may aid the development of single ion

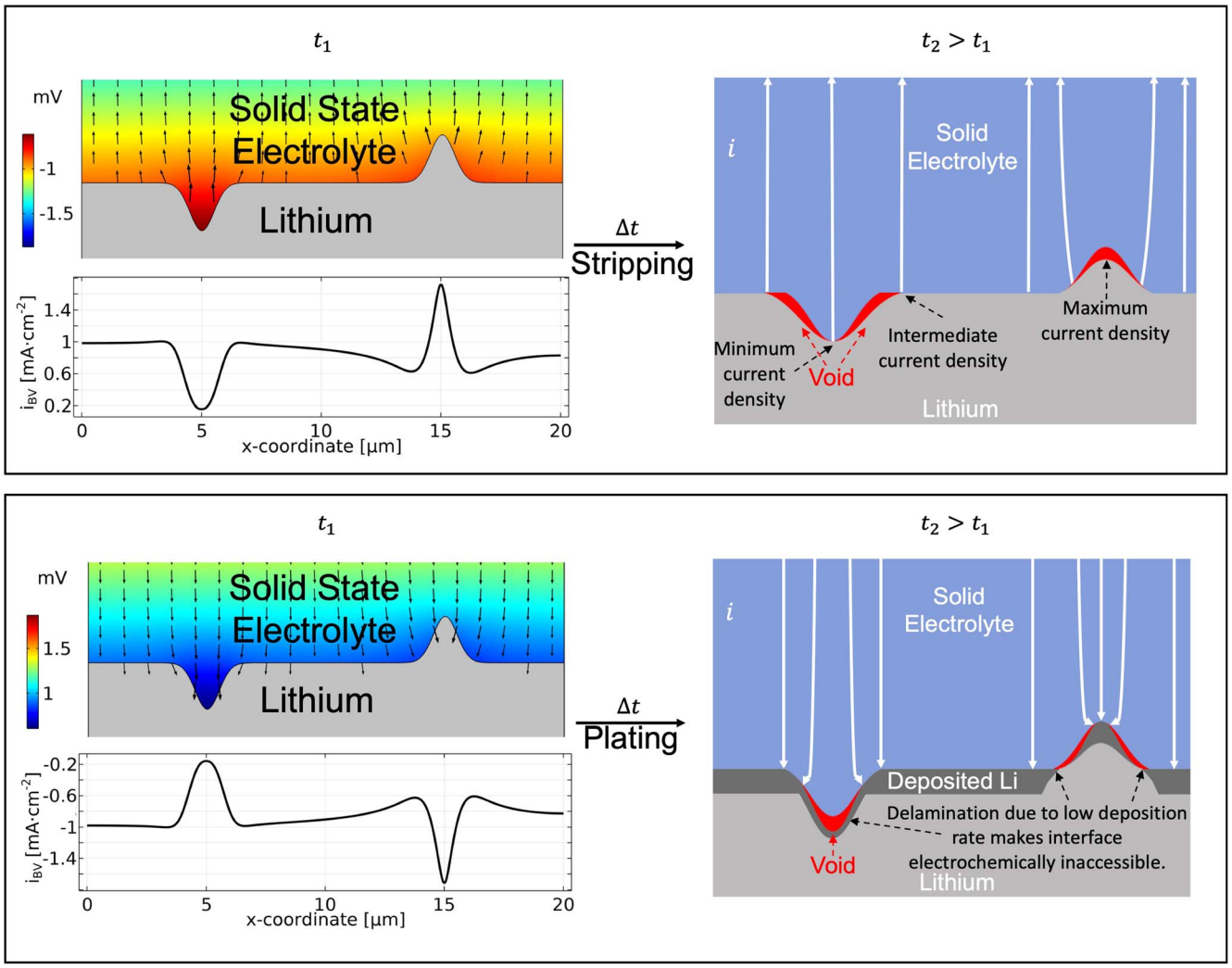

Figure 8. Stripping (a) and plating (b) at a Li/electrolyte interface at short (left panels) and long (right panels) times. The potential surface plots and interfacial current plots on the left are calculated using the developed model ($i_{applied}$ = 1 mA·cm^{-2}, κ = 1 mS·cm^{-1}), and the panels on the right are qualitative illustrations after extended periods of stripping/plating. The dark grey indicates freshly deposited lithium, and the red areas represent voids.

conductor / solid electrolyte interfaces that demonstrate improved plating and stripping at high current densities and areal capacities. Interfaces that are flat and without high-curvature peaks or valleys should result in more uniform current distribution, which provides an additional perspective on the superior cycling performance of flat, film-based separators (e.g., sputtered LiPON) versus particle-based separators (e.g., polycrystalline LLZO) in some conditions.

Acknowledgments

This work was supported by the U.S.-Israel Energy Center program managed by the U.S.-Israel Binational Industrial Research and Development (BIRD) Foundation.

Appendix

Starting from the equilibrium conditions across an undeformed surface defined by Newman and Monroe:

$$p^{\alpha'} = p^{\beta'} \qquad [A\cdot1]$$

$$\mu_M^{\alpha'} = \mu_{M^{z+}}^{\beta'} + z_+\mu_{e^-}^{\alpha'} \qquad [A\cdot2]$$

where p is the pressure, z_+ is the valence of the cation, μ_i is the electrochemical potential of species i, and superscript $'$ denotes the undeformed state. The α phase represents the electrode, and the β phase represents the electrolyte. For the case of a deformed surface, the pressure condition is relaxed, and equilibrium is defined by:

$$\mu_M^{\alpha} = \mu_{M^{z+}}^{\beta} + z_+\mu_{e^-}^{\alpha} \qquad [A\cdot3]$$

Assuming small deformations to condensed phases and that the molar volumes are unaffected by these deformations, the authors obtain two equations for the change in chemical potential of the metal and the metal ion due to the deformation:

$$\mu_M^{\alpha'} - \mu_M^{\alpha'} = \bar{V}_M^{\alpha'}(p^{\alpha} - p^{\alpha'}) \qquad [A\cdot4]$$

$$\mu_{M^+}^{\beta} - \mu_{M^+}^{\beta'} = \bar{V}_{M^+}^{\beta'}(p^{\beta} - p^{\beta'}) \qquad [A\cdot5]$$

For the case of a single-ion conducting electrolyte, $\bar{V}_{M^+}^{\beta'} = 0$, allowing the entire equation to be reduced to 0.

An interfacial force balance in the normal direction yields:

$$n \cdot(n\cdot[\bar{\bar{\tau}}_d^{\alpha} - \bar{\bar{\tau}}_d^{\beta}]) + (p^{\alpha} - p^{\beta}) + 2\gamma H = 0 \qquad [A\cdot6]$$

These equations can be rearranged to find $\Delta\mu_{e^-}$. Using Eqs. A·2, A·3, and A·4, we obtain:

$$\Delta\mu_{e^-}^{\alpha,\alpha'} = \Delta\mu_M^{\alpha,\alpha'} = \bar{V}_M^{\alpha'}(p^{\alpha} - p^{\alpha'}) \quad [A\cdot7]$$

The interfacial force balance can be written for the undeformed and deformed states and reported in terms of the pressure in the electrode:

$$p^{\alpha'} = p^{\beta'} - n \quad \cdot(n\cdot[\tau_d^{\alpha'} - \tau_d^{\beta'}]) - 2\gamma H \quad [A\cdot8]$$

$$p^{\alpha} = p^{\beta} - n \quad \cdot(n\cdot[\tau_d^{\alpha} - \tau_d^{\beta}]) - 2\gamma H \quad [A\cdot9]$$

We subtract to obtain the following:

$$p^{\alpha} - p^{\alpha'} = (p^{\beta} - p^{\beta'}) + (-n \quad \cdot(n\cdot[\tau_d^{\alpha} - \tau_d^{\beta}]))$$

$$(+n \quad \cdot(n\cdot[\tau_d^{\alpha'} - \tau_d^{\beta'}])) \quad [A\cdot10]$$

Equation A·7 is substituted, and the expression is simplified to yield:

$$\Delta\mu_{e^-}^{\alpha,\alpha'} = \Delta\mu_M^{\alpha,\alpha'} = \bar{V}_M^{\alpha'}(\Delta p^{\alpha,\alpha^-}) \quad [A\cdot11]$$

$$= \bar{V}_M^{\alpha'}\{(\Delta p^{\beta,\beta'}) + (-n \quad \cdot(n\cdot[\Delta\bar{\bar{\tau}}^{\alpha,\alpha'} - \Delta\bar{\bar{\tau}}^{\beta,\beta'}]))\}$$

ORCID

Eric A. Carmona https://orcid.org/0000-0002-3902-091X
Paul Albertus https://orcid.org/0000-0003-0072-0529

References

1. E. Kazyak, R. Garcia-Mendez, W. S. LePage, A. Sharafi, A. L. Davis, A. J. Sanchez, K. H. Chen, C. Haslam, J. Sakamoto, and N. P. Dasgupta, *Matter*, **2**, 1025 (2020).
2. A. Sharafi, E. Kazyak, A. L. Davis, S. Yu, T. Thompson, D. J. Siegel, N. P. Dasgupta, and J. Sakamoto, *Chem. of Mater.*, **29**, 7961 (2017).
3. G. T. Hitz et al., *Mater. Today*, **22**, 50 (2019).
4. P. Barai, K. Higa, A. T. Ngo, L. A. Curtiss, and V. Srinivasan, *J. Electrochem. Soc.*, **166**, A1752 (2019).
5. L. Barroso-Luque, Q. Tu, and G. Ceder, *J. Electrochem. Soc.*, **167**, 070526 (2020).
6. T. Krauskopf, H. Hartmann, W. G. Zeier, and J. Janek, *ACS Appl. Mater. Interfaces*, **11**, 14463 (2019).
7. T. Krauskopf, R. Dippel, H. Hartmann, K. Peppler, B. Mogwitz, F. H. Richter, W. G. Zeier, and J. Janek, *Joule*, **3**, 2030 (2019).
8. B. Kinzer, A. L. Davis, T. Krauskopf, H. Hartmann, W. S. LePage, E. Kazyak, J. Janek, N. P. Dasgupta, and J. Sakamoto, *Matter*, **4**, 1947 (2021).
9. Q. Tu, L. Barroso-Luque, T. Shi, and G. Ceder, *Cell Rep. Phys. Sci.*, **1**, 100106 (2020).
10. Y. Ren, Y. Shen, Y. Lin, and C. W. Nan, *Electrochem. Commun.*, **57**, 27 (2015).
11. J. Kasemchainan, S. Zekoll, D. Spencer Jolly, Z. Ning, G. O. Hartley, J. Marrow, and P. G. Bruce, *Nat. Mater.*, **18**, 1105 (2019).
12. F. Shen, M. B. Dixit, X. Xiao, and K. B. Hatzell, *ACS Energy Lett.*, **3**, 1056 (2018).
13. T. Swamy, R. Park, B. W. Sheldon, D. Rettenwander, L. Porz, S. Berendts, R. Uecker, W. Craig Carter, and Y. M. Chiang, *J. Electrochem. Soc.*, **165**, A3648 (2018).
14. L. Porz, T. Swamy, B. W. Sheldon, D. Rettenwander, T. Frömling, H. L. Thaman, S. Berendts, R. Uecker, W. C. Carter, and Y.-M. Chiang, *Adv. Energy Mater.*, **7**, 1701003 (2017).
15. C. Monroe and J. Newman, *J. Electrochem. Soc.*, **152**, A396 (2005).
16. P. Barai, K. Higa, and V. Srinivasan, *J. Electrochem. Soc.*, **164**, A180 (2017).
17. E. A. Carmona, M. J. Wang, Y. Song, J. Sakamoto, and P. Albertus, *Adv. Energy Mater.*, **11**, 2101355 (2021).
18. P. Barai, K. Higa, and V. Srinivasan, *J. Electrochem. Soc.*, **165**, A2654 (2018).
19. E. G. Herbert, N. J. Dudney, M. Rochow, V. Thole, and S. A. Hackney, *J. Mater. Res.*, **34**, 3593 (2019).
20. A. Mistry and P. P. Mukherjee, *J. Electrochem. Soc.*, **167**, 082510 (2020).
21. C. Monroe and J. Newman, *J. Electrochem. Soc.*, **151**, A880 (2004).
22. J. Newman and T. W. Chapman, *AIChE J.*, **19**, 343 (1973).
23. M. Z. Bazant, *Acc. Chem. Res.*, **46**, 1144 (2013).
24. M. Ganser, F. E. Hildebrand, M. Klinsmann, M. Hanauer, M. Kamlah, and R. M. Mcmeeking, *J. Electrochem. Soc.*, **166**, 167 (2019).
25. M. Wang, J. B. Wolfenstine, and J. Sakamoto, *Electrochim. Acta*, **296**, 842 (2019).
26. E. J. Cheng, A. Sharafi, and J. Sakamoto, *Electrochim. Acta*, **223**, 85 (2017).
27. H. Koshikawa, S. Matsuda, K. Kamiya, M. Miyayama, Y. Kubo, K. Uosaki, K. Hashimoto, and S. Nakanishi, *J. Power Sources*, **376**, 147 (2018).
28. C. G. Haslam, J. B. Wolfenstine, and J. Sakamoto, *J. Power Sources*, **520**, 230831 (2022).
29. A. Masias, N. Felten, and J. Sakamoto, *J. Mater. Res.*, **36**, 729 (2021).
30. A. Masias, N. Felten, R. Garcia-Mendez, J. Wolfenstine, and J. Sakamoto, *J. Mater. Sci.*, **54**, 2585 (2019).
31. W. E. Tenhaeff, E. Rangasamy, Y. Wang, A. P. Sokolov, J. Wolfenstine, J. Sakamoto, and N. J. Dudney, *ChemElectroChem*, **1**, 375 (2014).
32. W. S. LePage, Y. Chen, E. Kazyak, K.-H. Chen, A. J. Sanchez, A. Poli, E. M. Arruda, M. D. Thouless, and N. P. Dasgupta, *J. Electrochem. Soc.*, **166**, A89 (2019).
33. S. Kalnaus, A. S. Westover, M. Kornbluth, E. Herbert, and N. J. Dudney, *J. Mater. Res.*, **36**, 787 (2021).
34. A. S. Westover, N. J. Dudney, R. L. Sacci, and S. Kalnaus, *ACS Energy Lett.*, **4**, 651 (2019).
35. D. S. Jolly, Z. Ning, J. E. Darnbrough, J. Kasemchainan, G. O. Hartley, P. Adamson, D. E. J. Armstrong, J. Marrow, and P. G. Bruce, *ACS Applied Mat. & Interfaces*, **12**, 678 (2019).
36. V. Raj, V. Venturi, V. R. Kankanallu, B. Kuiri, V. Viswanathan, and N. P. B. Aetukuri, *Nat. Mat.*, **21**, 1050 (2022).
37. H. Yan et al., *Adv. Energy Mater.*, **12**, 2102283 (2022).
38. J. A. Lewis et al., *Nat. Mat.*, **20**, 503 (2021).